Numerical Wave Modeling in Conditions with Strong Currents: Dissipation, Refraction, and Relative Wind

FABRICE ARDHUIN,* ARON ROLAND,+ FRANCK DUMAS,# ANNE-CLAIRE BENNIS,# ALEXEI SENTCHEV,@ PHILIPPE FORGET,& JUDITH WOLF,** FRANÇOISE GIRARD,++ PEDRO OSUNA,## AND MICHEL BENOIT@@

* *Ifremer, Laboratoire d'Océanographie Spatiale, Plouzané, France*
+ *Technological University of Darmstadt, Darmstadt, Germany*
# *Ifremer, Laboratoire PHYSED, Plouzané, France*
@ *Laboratoire d'Océanologie et Géosciences (CNRS-UMR8187), Université du Littoral-Côte d'Opale, Wimereux, France*
& *Mediterranean Institute of Oceanography, CNRS, and Aix-Marseille University, and Sud Toulon-Var University, IRD, La Garde, France*
** *National Oceanographic Center, Liverpool, United Kingdom*
++ *Actimar SAS, Brest, France*
CICESE, Ensenada, Baja California, Mexico
@@ *Laboratoire Saint Venant, Chatou, France*

(Manuscript received 28 November 2011, in final form 9 July 2012)

ABSTRACT

Currents effects on waves have led to many developments in numerical wave modeling over the past two decades, from numerical choices to parameterizations. The performance of numerical models in conditions with strong currents is reviewed here, and observed strong effects of opposed currents and modulations of wave heights by tidal currents in several typical situations are interpreted. For current variations on small scales, the rapid steepening of the waves enhances wave breaking. Using different parameterizations with a dissipation rate proportional to some measure of the wave steepness to the fourth power, the results are very different, none being fully satisfactory, which points to the need for more measurements and further refinements of parameterizations. For larger-scale current variations, the observed modifications of the sea state are mostly explained by refraction of waves over currents and relative wind effects, that is, the wind speed relevant for wave generation is the speed in the frame of reference moving with the near-surface current. It is shown that introducing currents in wave models can reduce the errors on significant wave heights by more than 30% in some macrotidal environments, such as the coast of Brittany, in France. This large impact of currents is not confined to the locations where the currents are strongest, but also downwave from strong current gradients.

1. Introduction

Because he observed a rapid decay of wave energy facing an opposing current gradient, Phillips (1984) concluded that the dissipation of the wave energy could not be a linear function of the wave spectral density, which led him to propose a statistical description of breaking waves that could lead to a physically motivated expression for wave dissipation (Phillips 1985). Only recent evidence supported that the breaking probability could indeed be related in a nonlinear fashion to some measure of the spectral saturation (Banner et al. 2000). After several failed attempts (e.g., van Vledder and Hurdle 2002; Alves et al. 2003), parameterizations based on this saturation idea (van der Westhuysen et al. 2005; Ardhuin et al. 2009) have now shown a clear advantage over the linear parameterizations based on the statistical theory by Hasselmann (1974). Some recent work by Filipot and Ardhuin (2012) also demonstrated that a successful dissipation parameterization could be based explicitly on observed breaking wave statistics.

However, at regional scales the advantage of these new parameterizations is probably related to their built-in decoupling of wind sea growth from abnormal swell interference (e.g., Ardhuin et al. 2007), a feature that was already introduced by Tolman and Chalikov (1996).

Corresponding author address: Fabrice Ardhuin, Ifremer, Centre de Brest, 29200 Plouzané, France.
E-mail: ardhuin@ifremer.fr

DOI: 10.1175/JPO-D-11-0220.1

© 2012 American Meteorological Society

At global scales, the good performance of the Ardhuin et al. (2009) parameterization is largely due the introduction of a realistic nonlinear swell dissipation, which is the most important ingredient for obtaining low errors. Although breaking statistics are certainly nonlinear in terms of spectral parameters, it is not clear that a nonlinear parameterization of the whitecapping dissipation term produces better results.

Given the original argument by Phillips (1984), we found it interesting to go back to the effect of current gradients to look at the differences between parameterizations, from the laboratory scale to the scale of the coastal ocean. The present study is also an occasion to evaluate the accuracy of current effects in wave models, which has attracted only little attention.

Although many studies discuss the expected effect of currents on waves (e.g., Waseda et al. 2009), there are unfortunately very few validations of realistic numerical modeling of waves in currents, with the notable exception of Masson (1996) who used a specific model based on ray-tracing, without a full action balance. In fact, there is a very broad literature on theoretical effects of currents, from Barber (1949) to the review by Peregrine (1976). There are at least as many descriptions of numerical model results with more or less academic tests (e.g., Holthuijsen et al. 1991; Tolman 1991b; Benoit et al. 1996). Finally, the experimental evidence for current effects on waves is also abundant, from tidal currents (e.g., Vincent 1979; Ris et al. 1999; Wolf and Prandle 1999) to large oceanic currents like the Gulf Stream (e.g., Kudryavtsev et al. 1995). Unfortunately, in many cases there is only limited quantitative information about the current speed and spatial variation (e.g., Forget et al. 1995; Ris et al. 1999) or the waves (e.g., Haus 2007). For that reason we will not report here attempts at global numerical wave modeling with currents (e.g., Rascle et al. 2008), but only focus on experiments with relatively well known current fields.

Our investigation started in 2003, with a measurement campaign in the English Channel and the evaluation of four widely used numerical wave models. At that time, the conclusion was that taking into account currents improved the qualitative agreement between model and observed wave parameters, but the root-mean-square errors of the model results were actually larger with the currents (Girard-Becq et al. 2005). This was the occasion to fix some obvious problems in some of the numerical models used. In particular the artificial effect of swell on the wind sea growth, which is a common feature of the parameterizations derived from Komen et al. (1984), was found to be a problem. Taking advantage of improved wave model parameterizations and forcing fields, we now revisit the data from that experiment, with the addition of two other datasets that exhibit strong effects of currents on waves, and for which the current field is well known. These include the laboratory experiment by Lai et al. (1989), and macrotidal field data from the Iroise Sea (Ardhuin et al. 2009). Taken together, these three cases illustrate different situations in which currents have a strong influence on waves. These are a strong local dissipation, the far field of a refraction area, and the modifications in the local generation of waves. The general question that we are addressing here is as follows: do wave models today represent well the most important physical processes in the presence of strong currents? This question is largely independent of the choice of numerical model. Because all source terms are not implemented in all models, and to simplify the present paper, the results shown here were obtained with the Wind Wave Model II (Roland 2008), and WAVEWATCH III (Tolman 2009; Ardhuin et al. 2010), hereinafter abbreviated as WWMII and WWATCH.

2. Wave blocking and induced breaking

As waves propagate against an increasingly strong current, their group velocity can become less than the opposing current, so that the wave energy is unable to propagate upstream. In these cases the wave steepness generally gets large enough to induce breaking. Here we follow the assumption of (Chawla and Kirby 2002), which is largely supported by their experiments, that wave transformation through the blocking region is simply the result of propagation and dissipation associated with wave breaking. In that context, we investigate the effects of existing dissipation parameterization, and a possible support for the conclusions by Phillips (1984) that dissipation should be a strongly nonlinear function of the wave steepness. The potential numerical singularity is avoided in both WWATCH and WWMII by the use of spectral densities in the wavenumber–direction space and a variable wavenumber grid corresponding to fixed relative frequencies (Tolman and Booij 1998). For the other models that were compared by Girard-Becq et al. (2005), a particular treatment of the high frequency had to be added (M. Benoit 2007, personal communication—taken from presentation at the 2007 Globwave Meeting; available online at ftp://ftp.ifremer.fr/ifremer/cersat/documentation/presentations/2007/globwave_workshop/20070919_morning/Benoit.ppt). This consisted of enforcing an upper limit on the spectral level based on Hedges et al. (1985).

The blocking situation is investigated here using laboratory data by Lai et al. (1989). Because the global time step in WWATCH must be larger than 1 s, WWM II (Roland 2008) is used here to solve the wave action

equation and investigate the effects of various dissipation parameterizations.

a. Dissipation parameterizations

It is interesting to note that all dissipation parameterizations used here are quasi linear with a coefficient that multiplies the frequency-directional power spectrum of the surface elevation $F(f, \theta)$. This coefficient is proportional to a wave steepness ε to the fourth power or a higher power in the case of Alves and Banner (2003). However, this steepness is defined very differently between parameterizations.

In Komen et al. (1984), it is defined from the full wave spectrum

$$\varepsilon^{\mathrm{KHH}} = k_r H_s, \tag{1}$$

giving a dissipation source term

$$S_{\mathrm{oc}}^{\mathrm{KHH}}(f,\theta) = C_{\mathrm{ds}}\sqrt{gk_r}(k_r H_s)^4\left[(1-a)\frac{k}{k_r} + a\frac{k^2}{k_r^2}\right]F(f,\theta), \tag{2}$$

where H_s is the significant wave height, and k_r is a representative mean wavenumber defined by

$$k_r = \left[\frac{16}{H_s^2}\int_0^{f_{\max}}\int_0^{2\pi} k^r E(f,\theta)\,df\,d\theta\right]^{1/r}, \tag{3}$$

with $r = -0.5$ and $a = 0$ used by the WAMDI Group (1988), while Bidlot et al. (2005) used $r = 0.5$ and $a = 0.6$.

Phillips (1984) introduced a steepness that is local in frequency. This local steepness $\varepsilon^P(f)$ is proportional to $\sqrt{B(f)}$, where the nondimensional energy level $B(f)$ at that frequency (also called saturation) is defined by

$$B(f) = \int_0^{2\pi} k^3 F(f,\theta')C_g/(2\pi)\,d\theta'. \tag{4}$$

Such a local steepness only makes sense for a smoothly varying spectrum (Phillips 1984, p. 1428, column 2). Indeed for monochromatic waves of very small amplitudes $B(f)$ can be very large but is not associated to steep waves.

In this section we test three parameterizations based on Phillips (1984), and they mostly differ in the choice of the threshold B_r. In Alves and Banner (2003) S_{oc} is proportional to $(B/B_r)^4$, so that it increases steeply as B becomes larger than the threshold B_r, but it starts dissipating for $B < B_r$.

In the dissipation source functions of Ardhuin et al. (2010) and Babanin et al. (2010), B_r acts more like a switch and $S_{\mathrm{oc}}(f, \theta)$ is not such a high power of B,

$$S_{\mathrm{oc}}(f,\theta) = \sigma\frac{C_{\mathrm{ds}}^{\mathrm{sat}}}{B_r^2}[\max\{B(f) - B_r\}^2]F(f,\theta), \tag{5}$$

where C_{ds} is a nondimensional constant, B_r is a threshold for the saturation, and $F(f, \theta)$ is the spectral density of wave energy.[1] The minor differences between Babanin et al. (2010) and Ardhuin et al. (2010) include a different effect of wave directional distribution in the exact definition of B and a different formulation of the cumulative effect. In Babanin et al. (2010) this cumulative effect may dominate at lower frequencies than it does in Ardhuin et al. (2010). We also note that Ardhuin et al. (2010) is mostly derived from Banner and Morison (2006, 2010), which is not tested here, except for the smoothing of B over frequencies used by these latter authors. Finally, in Ardhuin et al. (2010) B is also a function of the wave direction, leading to a maximum dissipation in the mean wave direction, whereas Babanin et al. (2010) used a prescribed directional distribution of the dissipation which has a local minimum in the mean wave direction.

Compared to all other parameterization, based on a global or local steepness, Ardhuin et al. (2010) followed Tolman and Chalikov (1996) by including a separate swell dissipation term, but that effect is negligible at the scales, under 100 km, considered in the present paper.

b. Observations and model results

The laboratory flume of Lai et al. (1989) is 8 m long and 0.75 m deep, with a trapezoidal bar in the middle, with a height of 0.3 m (Fig. 1). Incident unidirectional waves with 95% of the energy between 1.5 and 2.0 Hz, these are relative frequencies, propagate along the channel. The incident spectrum is shown in Fig. 2. The relative peak frequency is at 1.9 Hz. The bar accelerates the opposing current from 0.12 to 0.18 m s^{-1}. The maximum current velocity, constant over the flat part of the bar, is enough to block all waves with an incident absolute frequency shorter than 2.1 Hz, for which the group speed over the bar is equal to the current velocity. This corresponds to a relative frequency of 2.7 Hz at the P1 wave gauge. According to geometrical optics, that is, neglecting diffraction and nonlinear effects, about 25% of the incoming energy flux is carried by waves with frequencies below 2.1 Hz and may propagate across the bar. The incoming significant wave height, here 0.3 m, should be strongly reduced, and waves are expected to be dissipated because of breaking, or reflected by the

[1] Here we use the TEST441 version of the parameterization described in that paper. The number 441 has no particular meaning and only serves to differentiate the different adjustment of parameters.

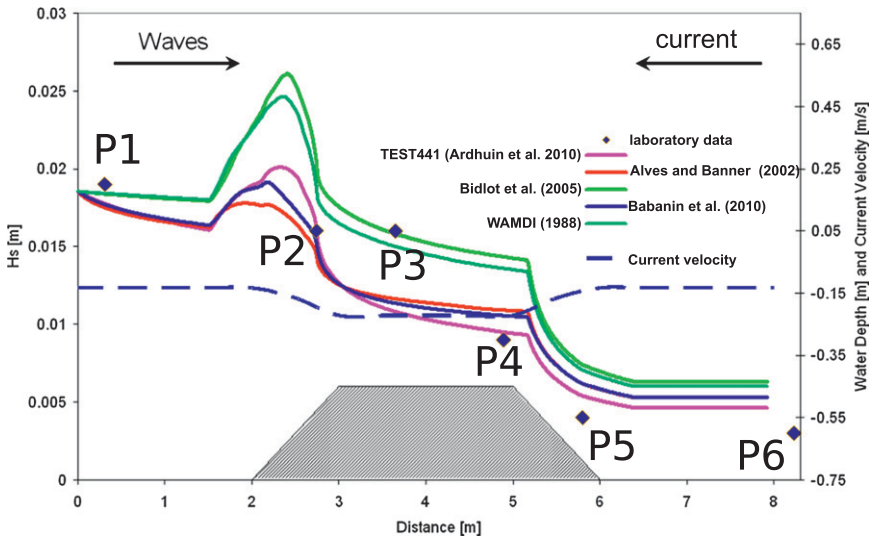

FIG. 1. Wave model results for the Lai et al. (1989) laboratory test, with waves against a varying current. (a) Observed and modeled significant wave heights, with a wide range of parameterizations. (b) Observed and modeled wave spectra. The top thin lines are the result using the parameterization by Bidlot et al. (2005), the middle thick line are the results using the TEST441 parameterization, based on Phillips (1984) and described in Ardhuin et al. (2010), and the bottom dashed lines are the observations. Observed spectra were transformed from the absolute reference frame of the laboratory, into the relative reference frame moving with the local current.

underwater topography (e.g., Ardhuin and Magne 2007), or weakened by the current via the work of the radiation stresses. The first process is believed to be dominant (Chawla and Kirby 2002), and thus should be reproduced by a proper parameterization of the dissipation induced by wave breaking.

As shown in Fig. 1, the discrete positions of the wave gauges do not give a full picture of the wave evolution, so that it is difficult to be certain that one parameterization is more realistic than another. However the most important result is the very clear difference between two groups of parameterizations.

For $x < 1.5$ m where the current is uniform the saturation-based parameterization give a decreasing wave height, caused by a significant dissipation, whereas the global-steepness parameterizations by the WAMDI Group (1988) and Bidlot et al. (2005), give a much lower level of dissipation. This initial dissipation is mostly associated with the shorter waves.

This adjustment stage is followed by an amplification of the wave height over the ramp, where the waves feel the strengthening of the opposing current. At the other end of the flume, for $x > 6$ m, the energy level is nearly constant for each parameterization, but it differs between them. We also note the energy at the end of the tank is generally overestimated in all model runs.

All parameterizations give almost the same results up to a frequency of 1.6 Hz, and strongly differ around the peak of the spectrum (Fig. 2). The global-steepness parameterization predicts a 40% increase in height before waves reach the P2 gauge, whereas the other group predicts a maximum increase of 12%. These different magnitudes can be clearly traced to the steepness definition. Indeed, the global steepness increases weakly when short waves get much steeper because it also includes the steepness of the longest waves in the spectrum, which are much less sensitive to the current gradient. Indeed, using $r = 2$ in the definition of k_r [Eq. (3)] would give the correct root-mean-square slope $k_r H_s/4$. For a broad spectrum, different wave scales have different slopes, but using $r = 0.5$ or even $r = -0.5$ as done by the WAMDI Group (1988) gives a mean steepness that emphasizes too much the long waves, which systematically underestimates the true wave slopes, and also underestimates its sensitivity to changes in the short wave spectrum. As a result, in the opposing current, the global-steepness parameterization does not enhance dissipation as much as the saturation-based parameterization, giving relatively higher waves.

We will now investigate how much this effect is relevant for oceanic conditions compared to other effects of currents. For comparison purposes we will only retain the global-steepness parameterization of Bidlot et al. (2005), because it is used operationally at European Centre for Medium-Range Weather Forecasts (ECMWF) for wave forecasting, and the saturation-based parameterization of

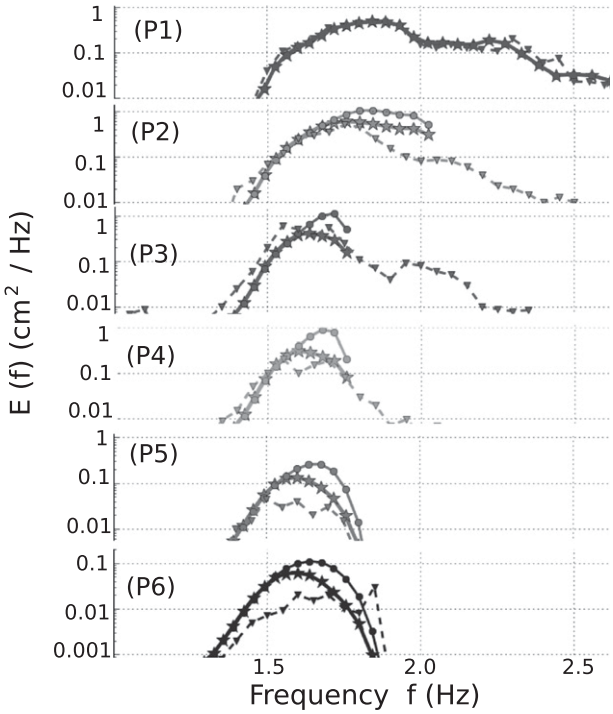

FIG. 2. (b) Observed and modeled wave spectra. The top thin lines are the result using the parameterization by Bidlot et al. (2005), the middle thick line are the results using the TEST441 parameterization, based on Phillips (1984) and described in Ardhuin et al. (2010), and the bottom dashed lines are the observations. Observed spectra were transformed from the absolute reference frame of the laboratory, into the relative reference frame moving with the local current.

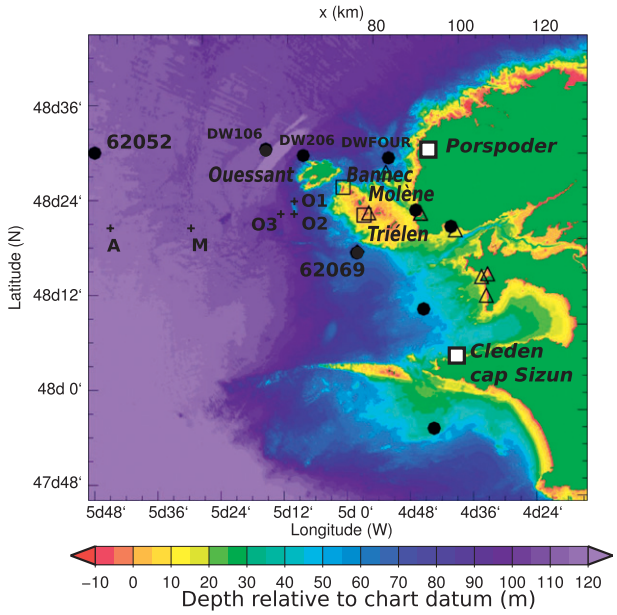

FIG. 3. Bathymetry of the Iroise Sea area. Large dots are the locations were waverider buoys have been deployed on several experiments. The buoys 62052 and 62069 (also called Pierres Noires) are part of the permanent wave monitoring network. Open symbols mark the locations where other sensors, pressure gauges or Nortek Vector current meters have been deployed by the Service Hydrographique et Oceanographique de la Marine (SHOM) for periods of a few months between 2004 and 2009. Among them, the buoy DWFOUR was deployed from September 2008 to March 2009. The locations of HF radar stations in Porspoder and Cleden Cap Sizun are also indicated.

Ardhuin et al. (2010), used operationnally at the National Centers for Environmental Prediction (NCEP) since May 2012.

3. Waves against strong tidal jets

In the ocean, currents are never uniform in the cross-stream direction, and thus other effects come into play, in particular the focusing of waves in the middle of opposed jets, caused by refraction. The capability of numerical models to represent the evolution of waves in currents is still poorly tested. Here we investigate the impact of very strong currents, up to 4 m s^{-1}, on storm waves measured off the west coast of France (Fig. 3).

Our area of interest is the Iroise Sea, with a spring tidal range of 6 m. Currents are strongly dominated by tides, which makes them well predictable, with a near-inertial component driven by winds and waves that only accounts for a few percent of the current variance (Ardhuin et al. 2009) and a magnitude of the order of 2% of the wind speed. Tidal currents in this area are also nearly depth-uniform, with a typical Ekman spiral due to bottom friction that is confined near the bottom. During summer, a density stratification is present (e.g., Le Boyer et al. 2009), which affects the wind-driven currents (Ardhuin et al. 2009) but has little effect on the tidal currents. Indeed, current profilers have been deployed in several measurement campaigns in the area, from 2004 to 2011 in depths ranging from 20 to 120 m. In all cases, currents are highly coherent over the water column, in particular in the top 70%, with tidal currents generally having a fairly uniform profile while the bottom 10 m are well approximated by a logarithmic profile $\log(z/z_0)$ with a roughness $z_0 \simeq 1$ cm. We shall thus assume that currents are uniform over the water depth. In particular they should be comparable with the near-surface measurements of high frequency radars.

For this we use the WWATCH model, based on the computer code by Tolman (2008), with the addition of advection schemes on unstructured grids, implemented by Roland (2008) and the use of new wave dissipation and generation parameterizations "TEST441" (Ardhuin et al. 2010). The triangle mesh used here is identical to the one already used by Ardhuin et al. (2009), and applied to routine forecasting as part of the Previmer

project (http://www.previmer.org), with a spectral resolution that includes 32 frequencies and 24 directions and a variable spatial resolution from 100 m to 5 km. Model grid and results are available online (http://tinyurl.com/iowagaftp/HINDCAST/IROISE).

This coastal model is forced by boundary conditions from a global multigrid system, with a resolution of 3.6 km in the Bay of Biscay. This global model has been carefully validated against altimeter data (Rascle et al. 2008; Ardhuin et al. 2011c) and generally gives accurate wave heights and mean periods, with normalized root-mean-square errors (NRMSEs) less than 10% for H_s. Directional properties have also been validated in detail by Ardhuin et al. (2011b), including effects of coastal reflection. Here the coastal reflection is not activated. Both models are driven by ECMWF wind analyses at 0.5 degree resolution and 6-hourly intervals, and currents and water levels from MARS model described below. To provide simplified measures of the difference between model time series X_{mod} and observations X_{obs} we use the following definitions for the normalized root-mean-square error (NRMSE),

$$\mathrm{NRMSE}(X) = \sqrt{\frac{\sum(X_{\mathrm{obs}} - X_{\mathrm{mod}})^2}{\sum X_{\mathrm{obs}}^2}} \tag{6}$$

and Pearson's linear correlation coefficient,

$$r(X) = \frac{\sum(X_{\mathrm{obs}} - \overline{X_{\mathrm{obs}}})(X_{\mathrm{mod}} - \overline{X_{\mathrm{mod}}})}{\sqrt{\sum(X_{\mathrm{obs}} - \overline{X_{\mathrm{obs}}})^2(X_{\mathrm{mod}} - \overline{X_{\mathrm{mod}}})^2}}, \tag{7}$$

where the overbar denotes the arithmetic average.

Some of the strongest currents are found in the Fromveur passage, between the islands of Ouessant and Bannec (Fig. 3) and wave blocking is easily observed, although measurements are more difficult. Indeed the current exceeds 3 m s^{-1} during neap tides (Fig. 4). This 3 m s^{-1} can block waves that, outside of the current jet, have periods of 7.6 s, while 2 m s^{-1} can block waves of 5 s. A typical situation occurred on 10 November 2008, when a strong southwesterly wind of 20 m s^{-1} generated wind seas against this current, while the dominant waves, an old wind sea, has a period of 12 s and mostly comes from the west. The model predicts a strong focusing of waves in the tidal jet and high wave dissipation rates in the center of this jet. This is a good occasion to test the differences given by saturation-based (Fig. 4b) or a Komen-type dissipation (Fig. 4c).

Away from the strong currents, the two maps in Figs. 4b and 4c are very similar. The offshore wave height is slightly higher in the TEST441 run because of a different balance between wind input, nonlinear fluxes, and dissipation. Since the dominant gradients in the wave heights and directions are due to island sheltering and refraction by the bathymetry and currents, the input and dissipation have a limited impact on the large scale wave height patterns.

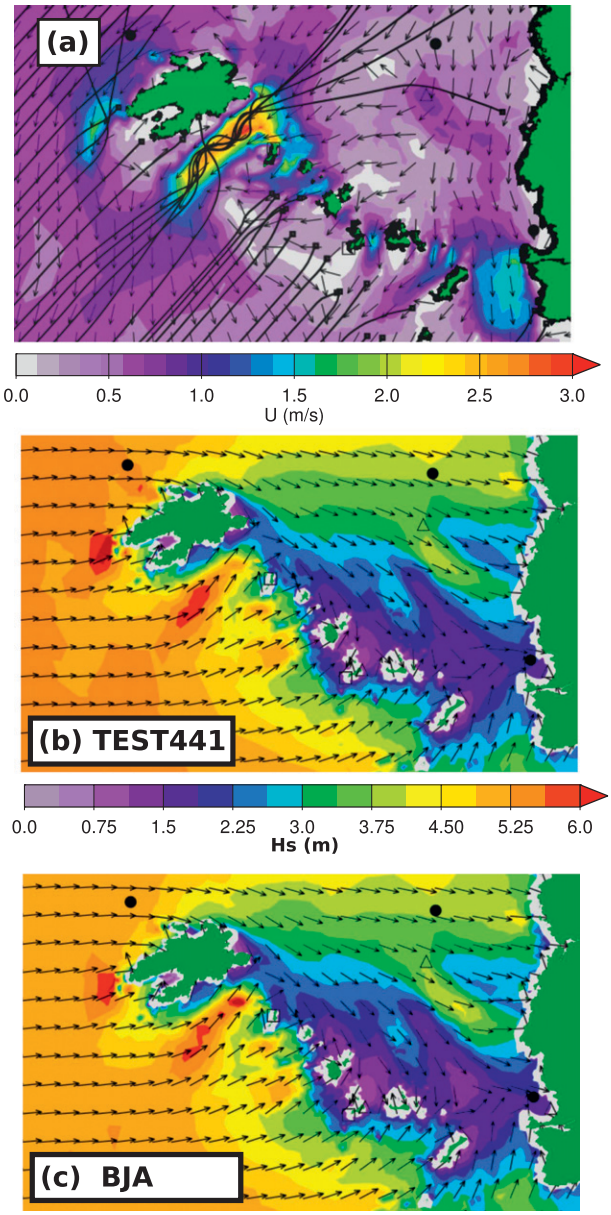

FIG. 4. Example of the modeled situation at 0500 UTC 10 Nov 2008, for which near-blocking is expected between Ouessant and Bannec islands. (a) Modeled currents and wave rays for 8-s waves from the southwest. (b) Modeled wave heights and directions using the TEST441 parameterization (Ardhuin et al. 2010), and (c) using the BJA parameterization (Bidlot et al. 2005). The gray areas are nodes that are treated as land, which generally agrees with the shoreline, which is the boundary of the green areas, with the addition of intertidal areas.

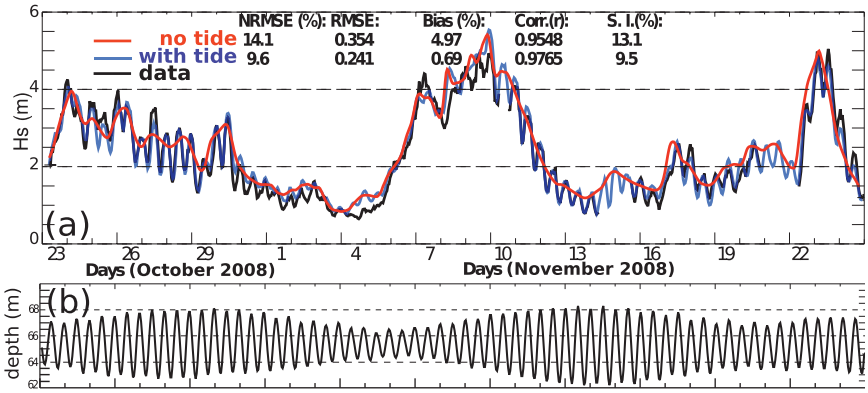

FIG. 5. (a) Typical time series of wave heights at the buoy 62069. The observed values are represented by the black solid line. Two model results are shown, one including currents and water levels in the model forcing (semitransparent blue), and the other without water levels and without currents (red), both use the TEST441 parameterization. (b) Modeled water level at the buoy.

However, in the area of strong current the saturation-based dissipation gives a maximum wave height that occurs upwave (to the southwest) of the maximum wave height given by the Komen-type dissipation term. As a result, H_s between Ouessant and Bannec reaches 6.5 m with the parameterization by Bidlot et al. (2005), whereas it is only than 5.3 m with the parameterization by Ardhuin et al. (2010) although it starts in that case from a slightly higher value offshore.

At buoy 62069, located south of the islands, the comparison of model results with data demonstrates that currents are very important for the sea states at that location. Figure 5 shows that the wave heights recorded at the buoy exhibit a modulation with a period of 12.5 h, related to the dominant M2 tide. The strength of the modulation varies with the neap/spring tide cycle, but is also influenced by the mean offshore wave direction. For example, a weaker modulation is recorded on 17 November (with westerly waves) compared to 30 October (with northwesterly waves) in spite of similar tidal amplitudes and dominant wave periods. The modulation can reach half of the observed mean value during spring tides with northwesterly waves. This figure also shows the difference between the model that includes currents and the model without current. This effect is not very sensitive to the choice of dissipation parameterization, and it is generally well captured by the model, with a considerable reduction in model error once the currents are taken into account. Over the month of data shown in Fig. 5, the NRMSE for H_s drops from 14.1% to 9.6% using hourly averaged H_s. Similar error reductions are found throughout the year.

Since the tidal modulation of the water depth is relatively small, the modulations are probably not due to the water level. But at the same time, the currents at the buoy 62069 are much weaker than in the vicinity of the islands. We shall see below that these stronger currents, up-wave from the buoy, cause a refraction pattern that influences the wave field at the buoy.

a. Data and model validation for current refraction

These currents have been mapped continuously since 2006 with a high frequency (HF) radar (WEllen RAdar, Helzel GmbH) operated at 12 MHz and designed by Gurgel et al. (1999). Given the measurement geometry, the resolution achieved by a standard processing of the data using beam forming from the 16-element receive antenna arrays is limited by the distance from the shore, in particular this processing may be too limited to resolve the very strong gradients around Ouessant and the Molène archipelago. To overcome this limitation, a direction finding processing using the Multiple Signal Classification algorithm (Schmidt 1986) has been applied for a few days of data, in combination with a variational regularizing algorithm (Sentchev et al. 2012). This processing achieves an azimuthal resolution of 1 km for the Porspoder radar station in the 2-km wide Fromveur passage, instead of 6 km using beam forming, in which case this passage is not resolved. We use both original and higher resolution processing to validate a numerical two-dimensional model of the area [Model for Applications at Regional Scales (MARS)], which is employed for forcing our numerical wave model. This model is used here in its two-dimensional version, solving the shallow water equations using a finite difference discretization, an alternate direction implicit (ADI) time stepping and high-order quickest scheme for advection. A full description of the model can be

TABLE 1. Statistical validation of modeled depth-averaged currents in the Iroise Sea using near-surface currents from the HF radar system using the standard beam-forming algorithm (top lines) over the full year 2008, at a selected list of locations (see Fig. 3), and, in the bottom lines, the reprocessed HF radar data, from 10 Jan to 29 Feb and 15 Jul to 20 Sep.

	r	r	NRMSE	NRMSE	Slope	Slope
Beam-forming data	U	V	U	V	U	V
Point A	0.92	0.96	39.3%	29.8%	0.89	0.87
Point M	0.88	0.97	48.2%	24.3%	0.82	0.93
Point DW106	0.95	0.97	31.7%	25.0%	0.92	0.88
Point O1	0.54	0.81	170.3%	90.2%	1.11	1.21
Point O2	0.45	0.91	175.1%	63.8%	0.95	1.26
Point O3	0.17	0.94	136.4%	43.5%	0.22	1.11
Reprocessed data						
Point A	0.92	0.94	40.4%	36.8%	0.86	0.98
Point M	0.86	0.95	53.1%	31.4%	0.81	0.91
Point DW106	0.96	0.96	32.8%	30.0%	0.91	0.83
Point O1	0.61	0.88	141.0%	52.5%	1.07	0.92
Point O2	0.45	0.93	133.0%	40.0%	0.85	1.00
Point O3	0.52	0.96	80.6%	34.1%	0.59	1.08

found in Lazure and Dumas (2008). The model is forced by sea surface elevation (at the boundaries) and atmospheric conditions (throughout the domain). Boundary conditions for the sea surface elevation are provided by a succession of four nested models with decreasing extensions from 5 km down to 300 m for the detailed model used here. The free-surface elevation is imposed along the open boundaries of the mother grid using the harmonic components provided by the FES2004 global tidal solution (Lyard et al. 2006).

A statistical comparison for the entire year 2008 of hourly modeled and HF radar values for the zonal (U) and meridional (V) component of the current shows a general very good agreement with a 10% underestimation of the surface current magnitude by the barotropic model at offshore locations (points A and M, Fig. 3 and Table 1). However, the most relevant features for ocean waves are the horizontal gradients in the current field, and these are most prominent around the islands, where it is unclear that the model accuracy or the radar resolution are sufficient in the original processing. Apparently the model and radar agree well for the broad current vein north of Ouessant (point DW106), but the agreement is much poorer for the U component south of Ouessant (points O1–O3), in particular with the original beam-forming processing (Table 1).

The original processing of the HF radar data leaves many blanks in regions of strong current gradients, in particular between the islands (Fig. 6). These strong gradients make the Doppler spectrum broader and then the estimation of a current velocity over a large measurement cell is difficult. Between the point O1 and the island of Ouessant, the reprocessed data reveals a strong current toward the northwest at times around the low tide. This particular current branch will be important in our analysis of measured waves. Our numerical model agrees better with this reprocessed data (Table 1), although the errors on the U component remain significant, and the current between O1 and Ouessant is oriented to the west instead of northwest. Figures 6c,d show the rapid change in the current as it reverses between 1100 and 1200 UTC. Compared to the other current streams, the westward current is relatively stable and may thus influence wave propagation for several hours. In our wave model we shall use these modeled currents as a forcing.

b. *Observed and modeled tidal modulations of the sea state*

Except for the buoy deployed just north of Ouessant, the largest tidal modulations in all the data acquired in the area were found at the location of the Pierres Noires buoy [World Meteorological Organization (WMO) number 62069], where some measurements were made in 2006, and where a buoy was permanently installed in 2008. A typical time series of wave heights at that location is shown in Fig. 5.

These modulations are strongest for waves from the northwest, and occur for all swell and wind sea frequencies. At the buoy location the water level and tidal currents are almost in phase, as the tidal wave propagates alongshore. We now analyze both a full numerical solution of the wave action equation and also wave rays, based on a stationary current assumption. This assumption is relevant here given the 30 km propagation distance of deep water waves across the largest currents, which takes only 40 min for 10 s waves. The full solution corresponds to results ''with tide'' shown on Fig. 4 and, focusing on four days only, the ''full tide'' results in Fig. 7.

The model was run with and without currents and water levels. Figure 7 shows that model runs without current completely miss the strong modulation of wave heights at the two buoy locations 62069 and DWFOUR. Changes in the water depth have a very limited influence at these buoy locations, given their mean water depth of 60 and 65 m, respectively. Adding currents in the wave model forcing reduces the error by more than 30% at both buoys, from a scatter index of 16.5% to 8.3% at 62069, and 17.6 to 12.4 at DWFOUR, over the four days starting on 26 October. Similar error reductions are found year-round at 62069 where we have a continuous record since 2007. This error reduction occurs in spite of relatively weak local currents, always less than 0.7 m s^{-1}, with weak local gradients. In fact, the modulation pattern can be easily explained by ray-tracing diagrams. These

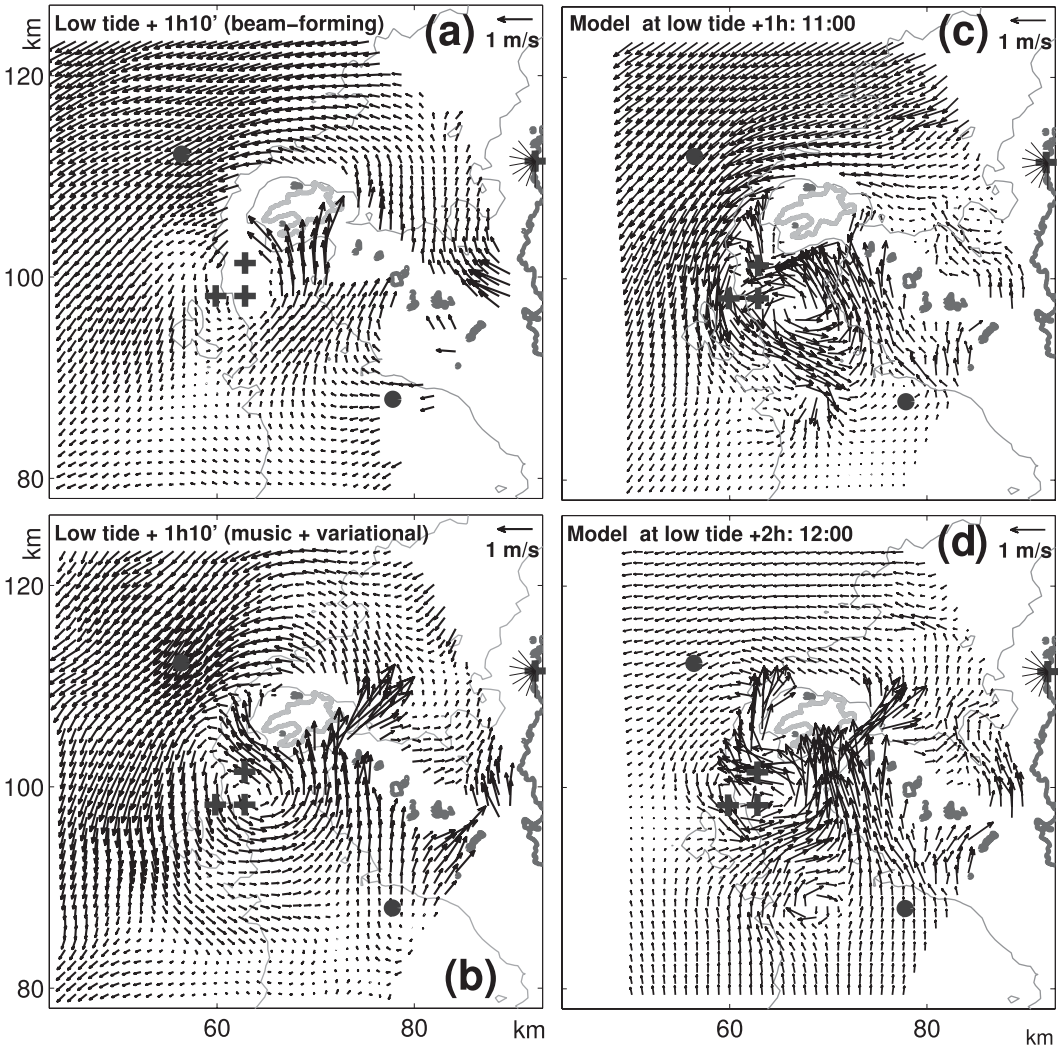

FIG. 6. Measured surface current 70 min after low tide, on the morning of 28 Oct 2008. The measurements are integrated over 20 min, from 1100 to 1120 UTC. (a) Shows the currents obtained with the original beam-forming, while (b) is given by the analysis technique of Sentchev et al. (2012), which combines a Multiple Signal Classification Schmidt (1986) direction-finding algorithm, using the 16 antennas of each receiving station, and a variational method to fill in holes and regularize the solution. Dots indicate the positions of buoys DW106 and 62069, and crosses are there to help the comparison of the two panels, at the positions of points O1–O3 for which errors statistics are given in Table 1. Gray lines show 50- and 100-m depth contours. For comparison, snapshots of the MARS model output at (c) 1100 and (d) 1200 UTC are shown.

rays were computed from parallel offshore directions, using the code by Dobson (1967), already adapted by O'Reilly and Guza (1993) and Ardhuin et al. (2001). Here we further take into account the turning of wave packets by the current, the advection of these packets by the current, and the change in relative frequency $\sigma = \omega - \mathbf{k} \cdot \mathbf{U}$, keeping the absolute frequency ω constant. In the case of stationary conditions, the ray equations are identical to the propagation equations, before discretization, that are solved by WWATCH [Eqs. (2.9)–(2.11) in Tolman (2009)]:

$$\dot{\mathbf{x}} = \mathbf{C}_g + \mathbf{U}, \tag{8}$$

$$\dot{k} = -\frac{\partial \sigma}{\partial d}\frac{\partial d}{\partial s} - \mathbf{k} \cdot \frac{\partial \mathbf{U}}{\partial s}, \quad \text{and} \tag{9}$$

$$\dot{\theta} = -\frac{1}{k}\left(\frac{\partial \sigma}{\partial d}\frac{\partial d}{\partial m} - \mathbf{k} \cdot \frac{\partial \mathbf{U}}{\partial m}\right), \tag{10}$$

where $\mathbf{x}$ is the horizontal position along the ray, θ is the local intrinsic wave direction, $\mathbf{C}_g$ is the vector intrinsic group speed, pointing in direction θ, s is a coordinate in

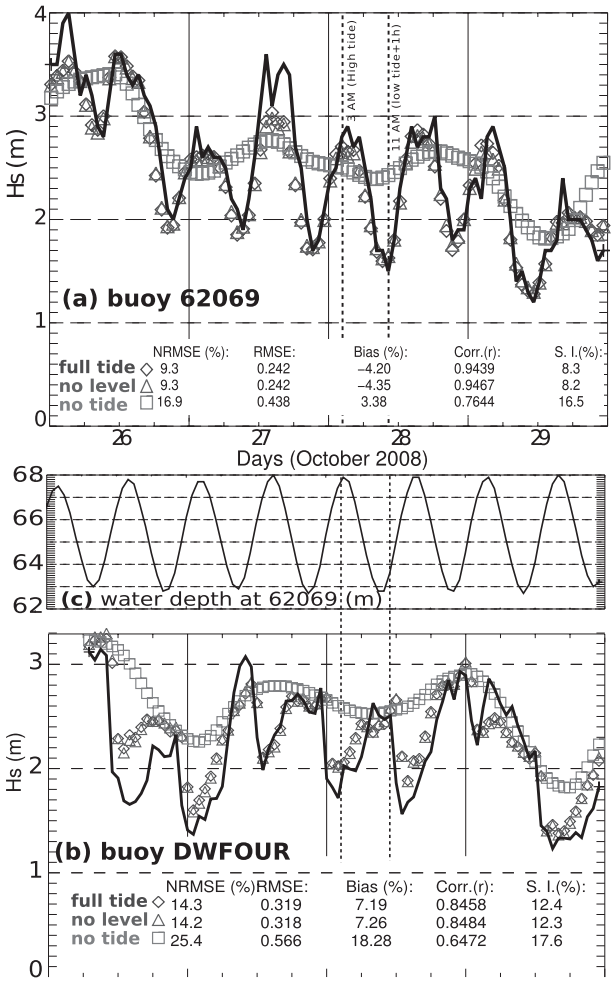

FIG. 7. Observed (solid line) and modeled wave heights at the buoy (a) 62069 and (b) DWFOUR (see Fig. 3) from 26 to 29 Oct, taking into account both water levels and currents (full tide, blue diamonds), only the currents (no level, green triangles), or no tidal effects at all (no tide, red squares, meaning that the water level is fixed and the currents are set to zero). (c) Modeled water level at 62069. Error statistics correspond to the data shown on the figure.

the direction θ and m is a coordinate perpendicular to s.[2] These ray equations are the same as those used by Mathiesen (1987), with the addition of finite depth and bottom refraction effects. The numerical treatment of the ray equations in WWATCH differs from ray tracing because of finite difference approximations. Also, in the ray tracing performed here, we do not attempt to recover wave heights, which would require a large number of ray calculations for each spectral component, typically using backward ray tracing (e.g., O'Reilly and Guza 1991; Ardhuin et al. 2001). Instead, our ray computations are only meant to illustrate and explain the main areas of wave energy focusing and defocusing.

At high tide, rays from the northwest that pass south of Ouessant are focused less than 10 km up wave from the 62069 buoy (Fig. 8a), which explains the relatively higher wave heights in that region (Fig. 8b). The rays that pass north of Ouessant tend to focus along the mainland coast at Corsen point, or further north, with a defocusing area around buoy DWFOUR. This propagation effect explains the pattern of modeled and observed wave heights at the buoy locations.

At times close to the low tide, rays in Fig. 8e show that the westward current jet, which develops south of Ouessant is responsible for trapping waves from the northwest, while the main current branch is orienter southward and deflects waves to the south, which is not the case in the absence of currents (Fig. 8c). The impact of the current in terms of wave height is clearly seen by comparing the calculations without current (Fig. 8d) and the calculations with current (Fig. 8f). The currents to the south of Ouessant are not an artifact of the flow model, and are rather well observed by the radar (Fig. 5a). Refraction over these currents casts a shadow area (where ray spacing increases) around the location of buoy 62069, resulting in lower wave heights. This pattern is sensitive to the offshore wave direction and is most pronounced for northwesterly waves.

A similar pattern occurs north of DWFOUR, but with the opposite tidal phase, resulting in higher waves at low tide at DWFOUR.

Current effects are also clear in the wave directions recorded at 62069, with a mean direction almost from the west at the low tides from 26 October to 29 October, veering by over 20 degrees to the northwest at high tide, when this direction is not blocked anymore by the currents south of Ouessant (Fig. 9). Around the time of the low tide, waves from the northwest have been refracted by currents and cannot reach the buoy, and the mean wave direction is from the west. This pattern is relatively well reproduced by the model. The only persistent bias in the model is found in the directional spreading which is underestimated by 6 degrees on average (not shown). This bias may be due to coastal reflection, not included here. Reflection over the current gradients (e.g., McKee 1978), may also contribute to the high directional spreads recorded by the buoys.

Because it is not the local current that has a strong effect on the waves and the current is weak at the buoy, the wave periods are not much affected, contrary to

[2] Due to the presence of the current, s differs from the along-ray direction.

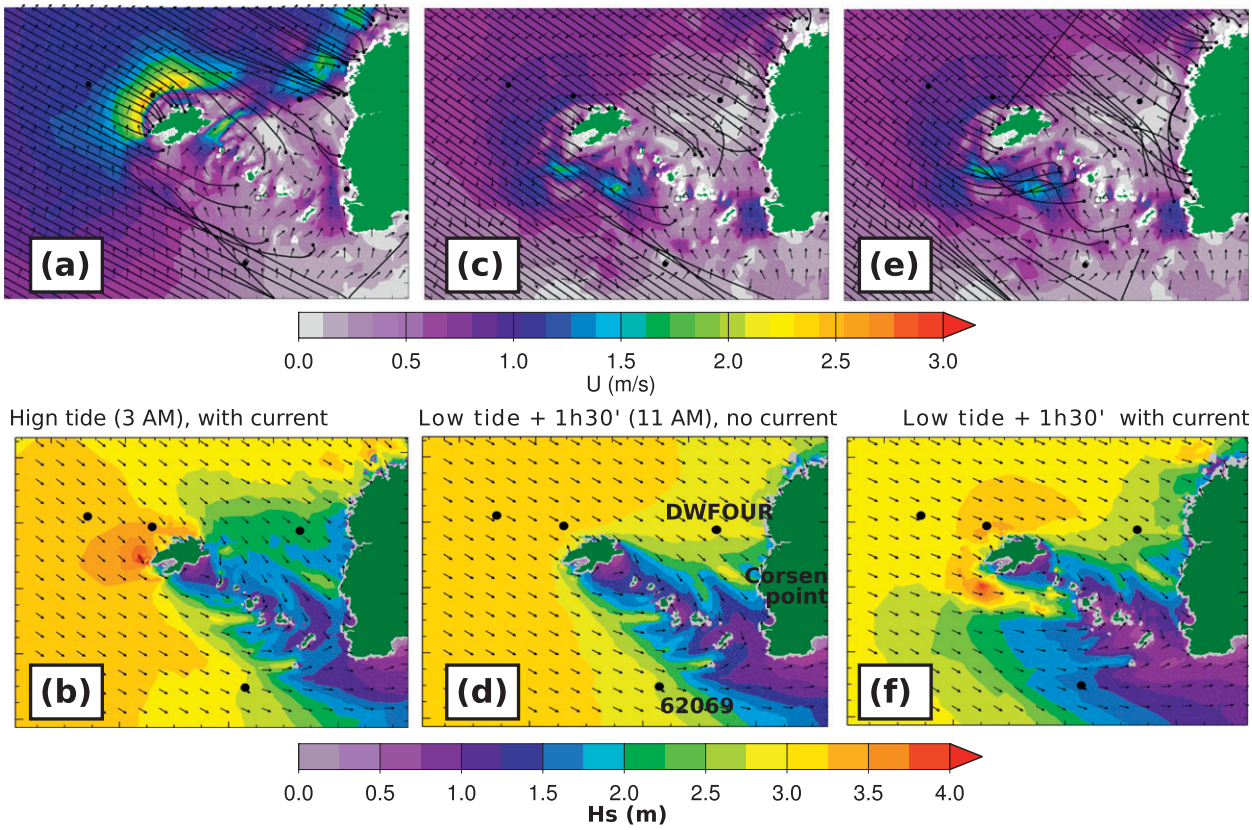

FIG. 8. (top) Current patterns around Ouessant and wave rays for a wave period of 10 s and (bottom) wave model results in terms of wave height and mean directions. These are shown for (a),(b) the 0300 UTC high tide on 28 Oct, where both rays and wave model take into account the currents and water levels (c),(d) 1.5 h after the 0930 UTC low tide of the same day, which corresponds to Fig. 5b, without taking into account the currents, and (e) at the same time and now taking into account the currents. In the top panels, colors indicate the magnitude of the current and the arrows show the current direction. Superimposed on these are rays for waves of 10-s period, starting from parallel directions in deep water. The black dots give the locations of buoys 62052, to the west, DW106 close to Ouessant, 62029 to the south and DWFOUR to the east, as also shown on Fig. 2.

other classical situations such as investigated by Vincent (1979), Battjes (1982), and Tolman (1991a).

Here, Fig. 10a shows that both observed and modeled mean frequency $f_{m0,-1}$ changes only by 5%–10% over the tidal cycle on the morning of 28 October, which is comparable to the modeled variation without currents nor water level changes (no tide) caused by the gradual evolution of the offshore wave field. A stronger variation is recorded for $f_{m0,2}$, which is weighted more heavily than $f_{m0,-1}$ toward the higher frequencies (Fig. 10b). Thus, one hour after low tide, the higher values of $f_{m0,2}$ at the buoy 62069, correspond to relatively higher energy levels for the short waves when the local current is oriented Northward, as shown in Fig. 6. This current opposed to the incident waves and wind results in some local enhancement of the shorter wave components, possibly due to changes in the effective fetch or in the apparent wind. These effects will be now discussed in more detail using a different dataset.

4. Local wind seas and currents

a. The 2003 experiment and our numerical model set-up

When wind seas are generated locally, the patterns of sea state can be significantly different because of the joint effects of wave generation and currents. Here we use data from an experiment carried out in 2003 in the western part of the Channel, with the purpose of investigating the capability of numerical wave models (Fig. 11a) and testing various techniques for measuring waves (Collard et al. 2005). An array of four Waverider buoys, two of them directional, was deployed along the swell propagation path from west to east (Fig. 11b). This array is located to the south of a wide area of shoals, Les Minquiers and the Chausey archipelago, that are dry at low tide, but with only a few rocks sticking out of the water at high tide. The experiment was carried out from early February to mid-March. The area is known for its

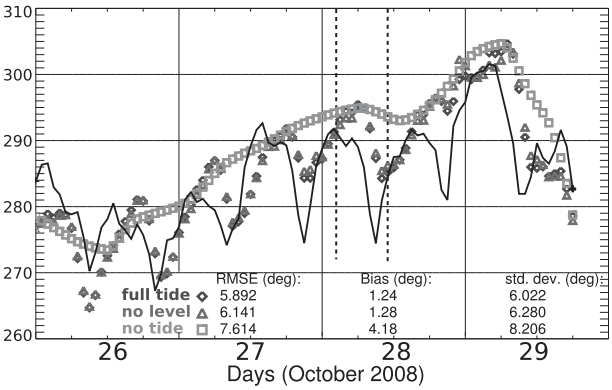

FIG. 9. Observed (solid line) and modeled mean wave direction at the buoy 62069.

very large tidal range, which exceeds 12 m during spring tides. The nonlinear tidal component M_4 is also particularly important with an amplitude that exceeds 30 cm in elevation (Chabert d'Hières and Le Provost 1970) and 14 cm s^{-1} for the east–west component of the surface current. This nonlinear tidal component makes the tidal currents strongly asymmetric with a larger flood velocity over a shorter time, as shown in Figs. 12a,c,d. The modeled current field is relatively homogeneous between buoys DW3 and DW4. Currents were measured with one ADCP, another one was unfortunately lost because of heavy fishing activities. A pair of very high frequency radars were deployed, operating at 45 MHz (Cochin et al. 2006; Sentchev et al. 2009). The vertical current profiles are typically logarithmic with a roughness length of a few centimeters, making the currents fairly uniform over the top 70% of the water column. Here again, because of the limited radar coverage, the radar data was used to calibrate the hydrodynamic model and check for biases and phase shifts in the modeled tidal currents and water levels. Root-mean-square errors on the current velocity was under 10 cm s^{-1} around buoy DW4, compared to a spring tide amplitude of 1.2 m s^{-1}, and the phase shift was less than 20 min for the dominant M2 tidal constituent (Girard-Becq et al. 2005).

The wave model contains 120 000 nodes that covers the full French Atlantic and Channel coastline with a resolution of 150 m along the shore. The part of the grid that covers the area of interest is shown in Fig. 11c. This model is forced by boundary conditions provided by the global multigrid system already used above, except that both global and coastal models are here forced by winds from the NCEP–National Center for Atmospheric Research (NCAR) Climate Forecast System Reanalysis (CFSR; Saha et al. 2010). Currents and water levels are again provided by the MARS model, but here the resolution is 3 km.

b. Tidal modulation of wave parameters

We focus here on the data recorded at the buoy DW3, located 6 km to the southwest of Chausey Island. From 17 to 20 February, a 8–15 m s^{-1} wind was blowing from the east–southeast (direction 120, Fig. 12), as moderate swells with peak periods larger than 10 s propagated from the west, into the Channel. For these days the tidal range is almost constant at 12 m. For the purpose of our analysis, we have separated the wave absolute frequency range into swell (0–0.12 Hz) and wind sea (0.12–0.5 Hz), which is appropriate for our case. Here we only show results with the TEST441 source term parameterizations (Ardhuin et al. 2010) because, for this case the Komen-type family of dissipation functions lead to an overestimation of the wind sea (Girard-Becq et al. 2005). This overestimation is largely caused by the presence of swell which reduces the mean steepness parameter defined by Eq. (1), leading to a strong reduction of the wind sea dissipation, as analyzed by Ardhuin et al. (2007).

Figure 13 shows the recorded strong modulation of the significant wave height, swell height, and wind-sea height over these 4 days. For the swell, the model results suggest that the change in water depth is indeed very important, but the model exaggerates the tidal modulation of wave heights. This model error may come from inaccurate modeling of swell evolution. In particular bottom friction is represented here by a linear parameterization with a constant $\Gamma = -0.067$ m^2 s^{-3} (e.g., WISE Group 2007), which gives a relatively strong damping of for low wave energies compared to a constant roughness parameterization (e.g., Ardhuin et al. 2003). Tests using a movable bed bottom friction and using a spatially varying sediment grain size give a more reasonable modulation of swell heights, but they also give a large positive bias (not shown).

We will now focus on the wind-sea heights, shown in Fig. 14c. The wind-sea height is maximum two hours after the peak in the flood current, and minimum two hours after the peak in the ebb current. On the second half of 19 February, the difference in height exceeds a factor of two over a tidal cycle from 0.5 to 1.15 m, with high values concentrated in a short time, and a longer minimum. Also, the fall in wave height from the maximum occurs faster than the rise from the minimum. Namely the time series exhibits both vertical and horizontal asymmetries.

The difference between the runs without current ("no cur") and the one without any tidal effect at all ("no tide") is the use of a variable water level in the former. This difference has very little impact on the short wind wave components. On the contrary, the tidal currents

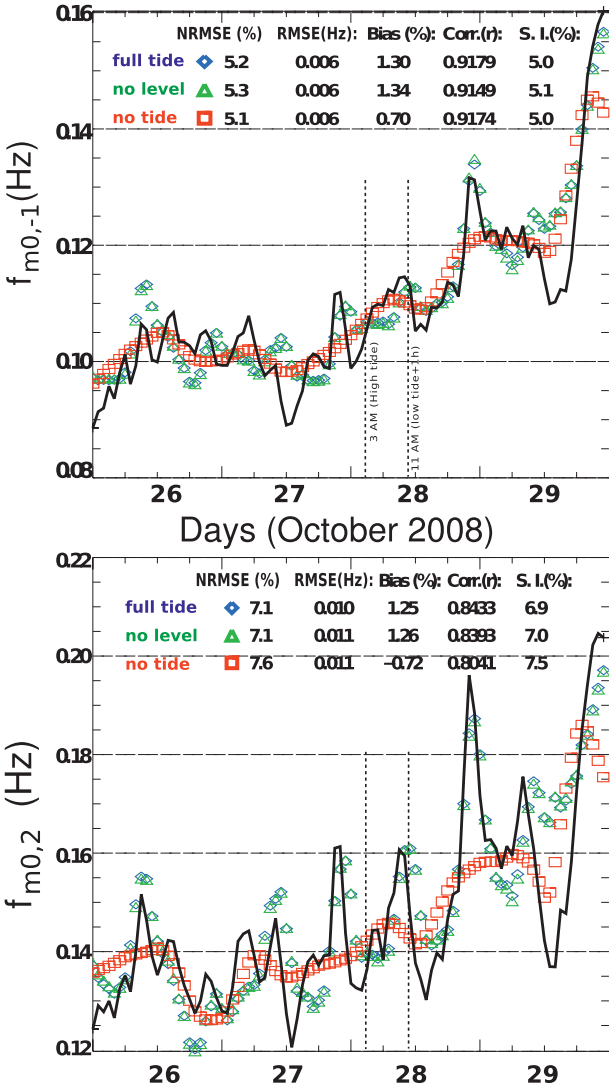

FIG. 10. Mean frequencies (a) $f_{m0,-1}$ and $f_{m0,2}$ modeled (symbols) and measured (solid line) at at the buoy 62069 in October 2008. Model results are shown, taking into account both water levels and currents (full tide), only the currents (no level), or no tidal effects at all (no tide). The vertical dashed lines mark the 0300 and 1100 UTC (high tide and low tide + 1 h) times that corresponds to the maps shown in Fig. 9.

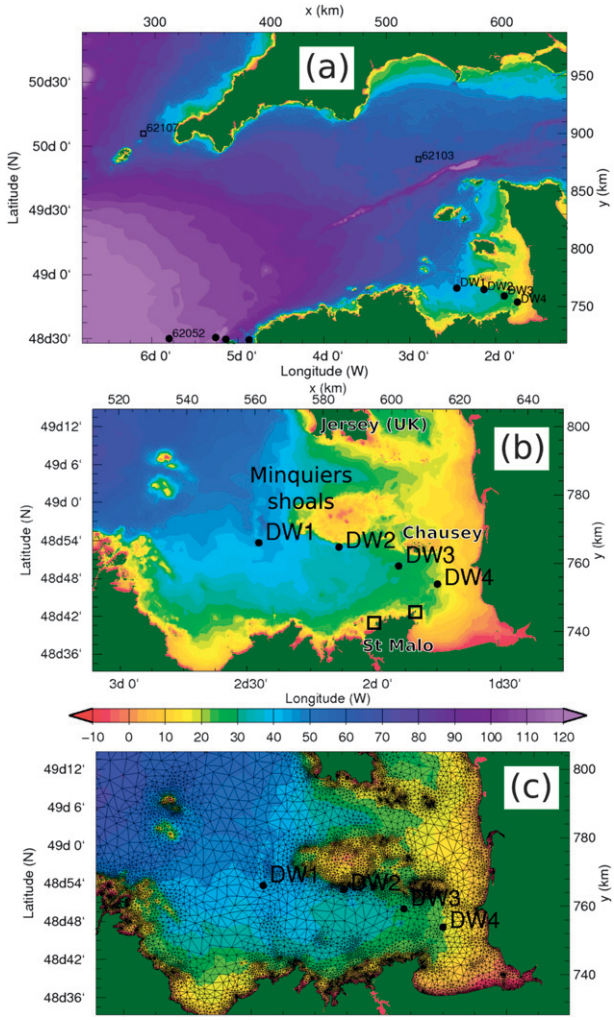

FIG. 11. (a),(b) Bathymetry of the Western Channel and location of buoy measurements during the 2003 experiment. The two squares indicate the VHF radar stations. (c) Mesh of the wave model in the area of interest. Water depths are relative to the mean sea level.

have a large influence on the wind sea evolution, which is clearly seen by the difference between the no cur run and the "RWIND = 0" run.

Another strong modulation is the evolution of the absolute peak wave frequencies, with a change by nearly a factor two, from 0.18 to 0.3 Hz, that exceeds the model results (Fig. 14). The wind-sea waves are shortest at low tide and become much longer and energetic at high tide. We also note that a significant level of energy exists at frequencies above 0.26 Hz that would have been blocked by the maximum current if the waves had been generated in an area with zero or following currents. This shows that these waves must be generated locally in the area of strong current. The overestimation of the peak frequency when the waves follow the current, here from low tide+3 h to high tide, is probably caused in part by the slow wave growth bias found at short fetch with the TEST441 parameterization (Ardhuin et al. 2010).

A simulation in which refraction due to both currents and bathymetry was deactivated gave a very large difference for the swell, with a wave height doubled, but virtually no difference in the wind sea, with a root-mean-square difference of 4% on the wind sea height, and less than 20% for the spectral densities. The effect of currents on the wind sea is thus caused by processes other than refraction.

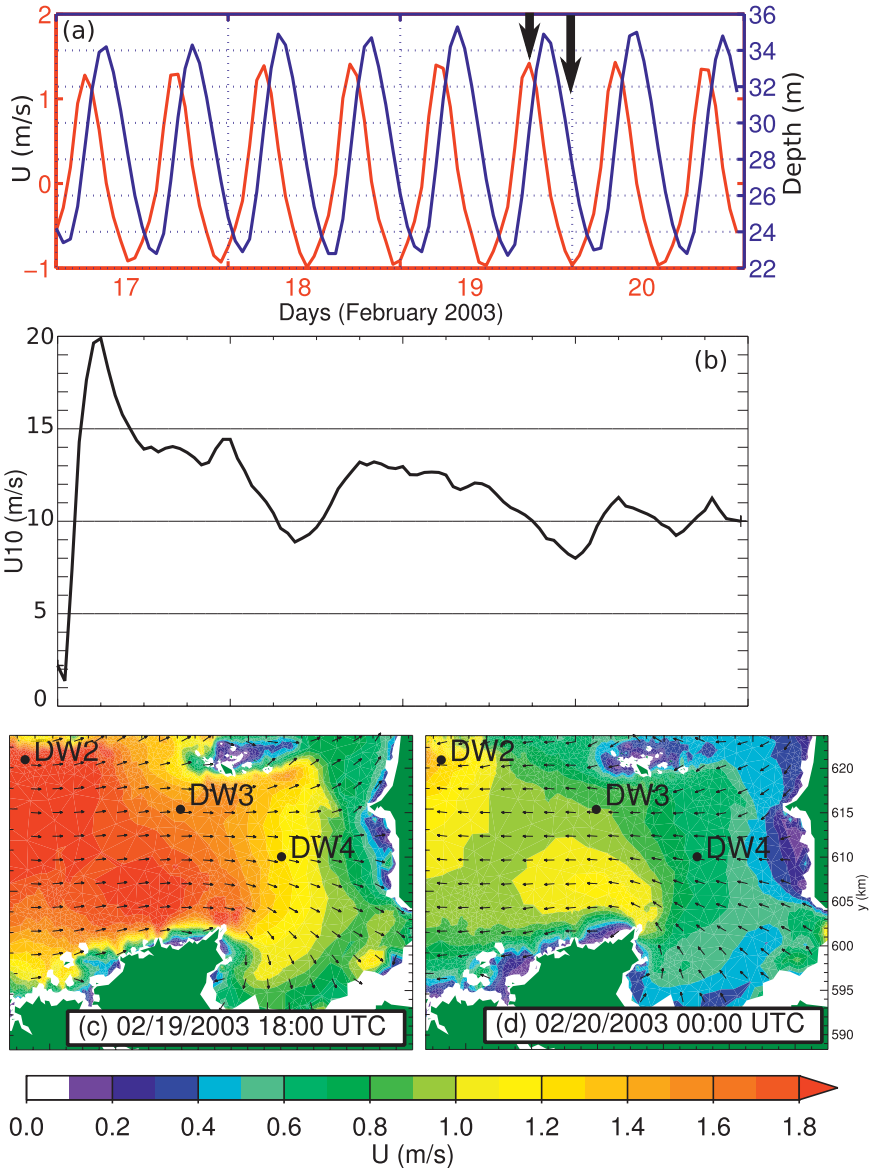

FIG. 12. Time series of (a) eastward current and tidal elevation, and (b) wind speed at 10-m height at the location of buoy DW3, according to NCEP–CFSR (Saha et al. 2010). The two thick arrows in (a) indicate the flood and ebb peak at DW3, (c),(d) times for which the modeled current fields are shown.

The current speed U between Chausey and Saint Malo reach 1.5 m s^{-1} oriented along the east–west direction with a very flat tidal ellipse (Cochin et al. 2006). With this high speed of the current in comparison to the wind, we investigated the importance of the ''relative wind effect'' as implemented in WWATCH. The model uses the difference of the two vector velocities, wind at 10-m height, and current, as the effective wind vector that generates the waves. This parameterization assumes that the atmosphere does not adjust to the presence of the current. Using a global coupled wave-atmosphere model, J. Bidlot (personal communication, 2011) found that using half the current speed would be better on average. Using the full current speed, as we do here can exaggerate the real effect because the relevant level at which the wind should be taken is not the standard 10 m height but rather the top of the atmospheric surface layer, where the wind is relatively larger. Also, the atmosphere adjusts to the change in surface stress so that the true winds are slightly reduced over opposing currents.

The relative wind effect is significant as revealed by the difference between diamonds and triangles in Fig. 13c,

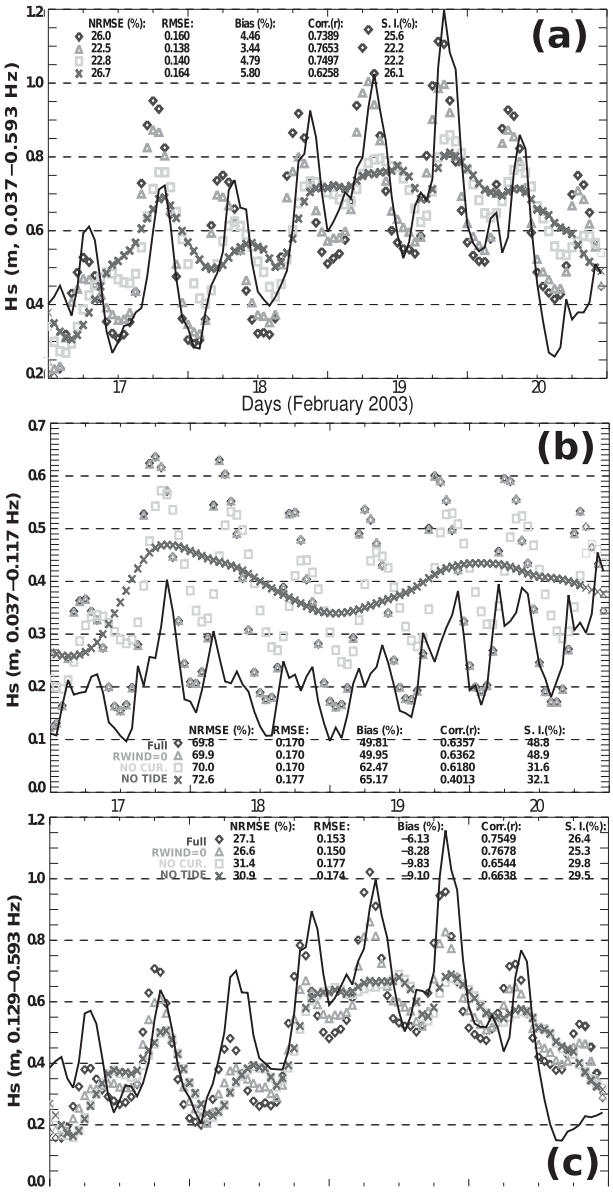

FIG. 13. (a) Significant wave height, (b) swell height, and (c) wind-sea height over four days in March 2003 at the buoy DW3. Observations are represented with the solid black line, and the various symbols represent model results. The full solution includes relative wind effects, currents, and water levels. The other runs deactivate these different options: "RWIND = 0" has no relative wind, "NO CUR." has no current, and "NO TIDE" has no variable water level nor current.

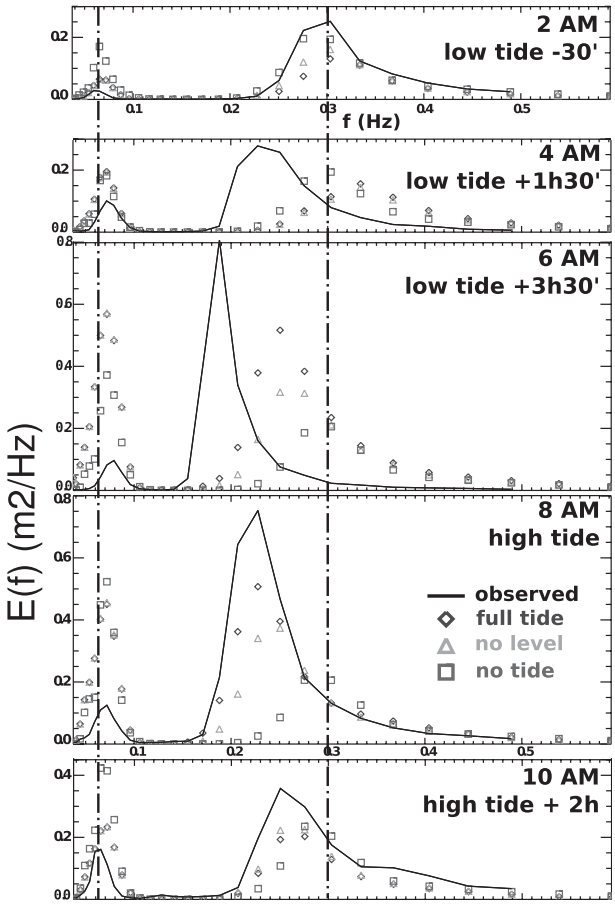

FIG. 14. Frequency spectra over one tidal cycle on the morning of 19 Feb 2003, at the location of buoy DW3.

accounting for about 25% of the observed modulation, even though the model may exaggerate the true effect.

c. A simplified model

To understand the magnitude of the changes in H_s over a tidal cycle, we have performed simplified numerical simulations with a rectangular flat bottom channel 40 km long and 20 km wide, taking a uniform current across the width of the channel, with a variation given by,

$$U = \{U_0 \cos[\omega_T(x/C_T - t)] + U_m\} \frac{1 + \tanh[(x - 3L)/L]}{2}, \tag{11}$$

where we have chosen a tidal radian frequency corresponding to the lunar semidiurnal tide, $\omega_T = 1.4 \times 10^{-4}\ \mathrm{s}^{-1}$. The tide propagation speed is given by the water depth, $C_T = \sqrt{gD}$ and we have taken $D = 30$ m. We will consider a wave train propagating toward $x > 0$ without any modulation in the region $x < 0$. The modulation is caused by the variable current which ramps up gradually, over a distance $L = 3.3$ km, from $U = 0$ to an oscillating value of amplitude U_0, so that the wave train can adjust smoothly to the current.

We first consider nearly monochromatic waves with a wave action $A = H_s^2/(16\sigma)$ where σ is the local intrinsic frequency, without any forcing, dissipation or nonlinear effects. Since we consider only short wind-waves they

are in deep water and their local wavenumber is $k = \sigma^2/g$ and the local intrinsic phase speed and group speed are $C = \sqrt{g/k}$ and $C/2$. The determination of the wave height thus reduces to the conservation of the number of waves and of the wave action (e.g., Phillips 1977),

$$\frac{\partial k}{\partial t} + \frac{\partial}{\partial x}[(C - U)k] = 0, \quad \text{and} \tag{12}$$

$$\frac{\partial A}{\partial t} + \frac{\partial}{\partial x}[(C/2 - U)k] = 0. \tag{13}$$

These are associated to initial conditions $k = k_0$, $A = A_0$, and a boundary condition at $x = 0$. The equations are linear with respect to H_s^2 so that we can choose a realistic boundary condition $H_{s0} = 0.2$ m and an initial frequency $f = 0.2525$ Hz.

This system of equations for the unknowns k and A has, to our knowledge, no analytical solution because of the nonlinearity in the advection of k. Given the current forcing and steady boundary conditions we expect a periodic regime to be established within one tidal period.

Vincent (1979) studied a relatively similar case with the advection of wind-waves by the tidal wave, but he chose to linearize Eq. (12) and looked for solutions that are spatially periodic, with a wavelength equal to the tide wavelength. Instead, we solve Eqs. (12)–(13) numerically using a second order upwind scheme on with a 300 m horizontal resolution and a time step of 13 s.

Exploring the effect of the current magnitude, we start from $U_0 = 0.1$ m s^{-1}. In the limit of low currents we find that, for our range of parameters, the modulation in wave height, defined as the maximum minus the minimum value divided by two, is

$$H_s - H_{s0} \simeq 2H_{s0}\alpha, \tag{14}$$

where $\alpha = U/C_0$. This is the same amplification that is found for $\alpha \ll 1$ in the steady case for waves propagating over a spatially varying current, given by,

$$\sigma = \sigma_0 \frac{1 - \sqrt{1 - 4\alpha}}{2\alpha}, \quad \text{and} \tag{15}$$

$$H_s = H_{s0}\sqrt{\frac{\sigma C_{g0}}{\sigma_0(C_g - U)}}. \tag{16}$$

This means that in practice the tidal period is long compared to the adjustment of the wave field.

After a few hours of transition from the initial conditions, the wave heights oscillate with a period equal to the tidal period. When the channel length is extend to 400 km, the solution is spatially quasi-periodic, with

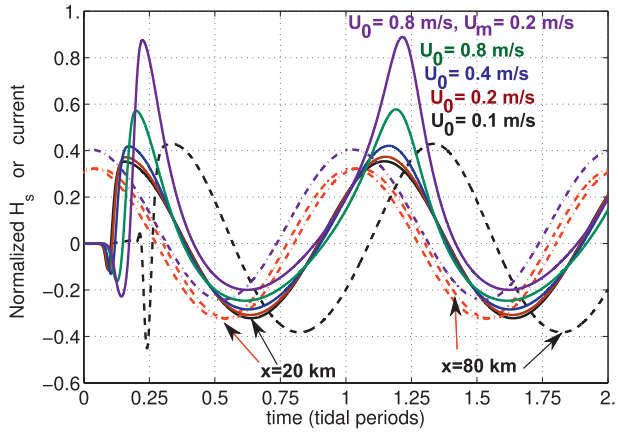

FIG. 15. Wave height modulations by an oscillating current obtained from a numerical solutions of Eq. (13). The solid lines show different results for H_s at $x = 20$ km obtained with different current amplitudes U_0 and offset U_m, as defined in Eq. (11). The plotted values of H_s are normalized as $(H_s - H_{s0})/(H_{s0}U_0)$, with U_0 in m s^{-1}. Namely, with our choice of $H_{s0} = 20$ cm, a current amplitude of $U_0 = 0.1$ m s^{-1} gives a modulation amplitude of 0.67 cm for H_s while $U_0 = 0.8$ m s^{-1} gives 6.5 cm. The dash-dotted lines show the current normalized as $U/(C_{g0}U_0)$, with U_0 in m s^{-1}. All curves are for $x = 20$ km except for the dashed curves which correspond to $x = 80$ km.

a wavelength close to 190 km, which is of the order of the 140 km expected for a disturbance that propagates at the average group speed of 3.1 m s^{-1}, and much less than the tidal wavelength of 770 km.[3] As a result, the tidal current field is practically uniform and its spatial propagation only introduces a small phase shift. The other consequence is that the maximum in wave height will lag the maximum of the opposing current, and this lag increases linearly with x. Figure 15 shows that the lag is already larger than 1.5 h for $x = 20$ km, similar to the values found at DW3. Associated with this lag, the decrease in wave height becomes gradually faster than the increase, giving a horizontal asymmetry that is visible in the black dashed curve of Fig. 15.

This horizontal asymmetry is much more pronounced for stronger currents. For finite current values, the changes in wave properties remain very close to the stationary solution at least for the short propagation distances. The same results were also obtained using WWATCH with the only effect that the curves are less smooth due the spectral discretization.

We now return to the more realistic situation where waves are generated by the local wind, instead of being propagated from a boundary, and we use a wind speed of

[3] It is not strictly periodic, as the shape of the H_s maximum becomes more asymmetric toward the end of the channel.

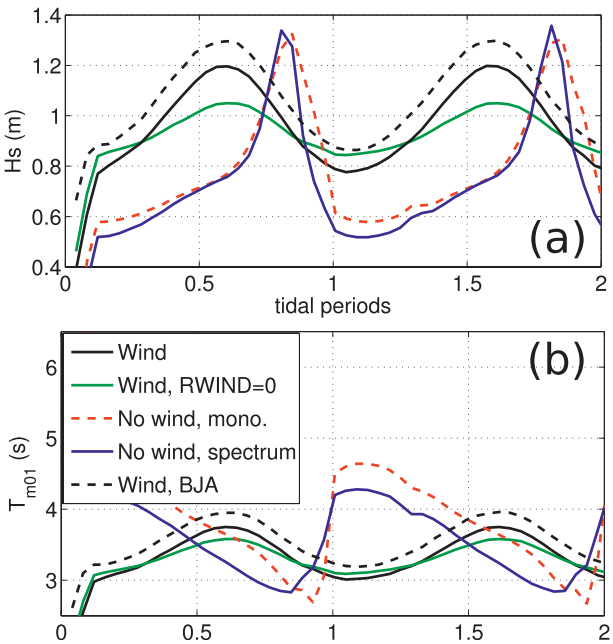

FIG. 16. (a) Wave height and (b) mean wave period modulations by an oscillating current, as computed by WWATCH at the centerline of a rectangular channel, 15 km in width, $x = 17$ km from the upwave boundary. All results are obtained with the same current oscillating sinusoidally from 1.5 (opposing) to -0.9 m s^{-1} along the mean wave direction. The wave field was either generated from rest by a 13 m s^{-1} wind, including the relative wind effect or not (RWIND = 0), or propagated from the boundary ("no wind") using a monochromatic spectrum of frequency 0.25 Hz or a Gaussian spectrum of standard deviation 0.025 Hz with, in that case, a directional distribution proportional to $(\max\{\cos\theta, 0\})^2$. Because of stronger blocking in that case the wave height at the upstream boundary is take to be 1.75 times larger for the broad spectral case. Finally, the simulation with wind was also repeated using the parameterization BJA (Bidlot et al. 2005) instead of TEST441 (Ardhuin et al. 2010).

13 m s^{-1} that is slightly larger than modeled at DW3, but produces an average peak frequency of 0.25 Hz at a fetch of 20 km, which roughly corresponds to the observed conditions. A gradual phase shift compared to the tide is still modeled and roughly corresponds to the wave height pattern propagating at the mean group speed. However, in such conditions, according to the model, the strength of the modulation is much reduced compared to the monochromatic wave propagation (Fig. 16a). More importantly, the mean wavelength maximum is now in phase with the wave height maximum whereas it was out of phase in the case of simple propagation (Fig. 16b). Indeed the short waves modeled without dissipation would be too steep and cannot exist. It thus appears that wave breaking is an important term for the shape of the spectra in these conditions. Still, the model results are qualitatively independent of the choice of parameterization for the wave generation and dissipation, as shown in Fig. 16 by the comparison of the solid and dashed black lines. Interestingly, the relative wind effect is stronger in this idealized model configuration than in the realistic modeling of the Saint-Malo area.

This asymmetric growth of the wind sea, stronger with opposing currents, is thus probably a combination of at least three effects. There is certainly some adjustment of the wave properties corresponding to the conservation of wave action over a time-varying current. However, the growth of the wavelength with the wave height cannot be explained by that effect, and thus there must be a strong growth of the wave field over the tidal cycle. Finally, the relative wind effect probably explains 20%–40% of the wave height modulation.

5. Conclusions

At global scales, the accuracy of numerical wave models is generally defined by, in decreasing order of importance, the accuracy of the forcing fields, the behavior of the physical parameterizations, and the accuracy of the numerical schemes used to integrate the wave action equation (Bidlot et al. 2007; Ardhuin et al. 2010, 2011a). Here we have investigated how models behave in the presence of strong currents, and this statement on model accuracy remains generally true. In particular, the accuracy of the forcing includes the current fields and its gradients.

At the shortest scales compared to the wavelength, a very rapid steepening of the waves against an adverse current leads to intense wave breaking and dissipation. All the parameterizations of wave breaking used here represent the dissipation rate as a steepness to the fourth power times the spectrum, but the different definitions of steepness can produce markedly different results. Parameterizations based on the saturation of the wave spectrum appear to be more realistic for the early stages of the wave evolution, but may not give the best solution everywhere. It is possible that the intermediate dissipation term proposed by Banner and Morison (2006) or Filipot and Ardhuin (2012), not completely local in frequency like the saturation formulations, nor global across the full spectrum like the dissipation terms derived from the Hasselmann (1974), should have an intermediate behavior. Experimental data with a higher spatial resolution, both in the laboratory and in the field will be needed to better resolve the full spatial evolution of the wave field and can be very useful to validate these parameterizations. At present, given the very good performance at global scales of the saturation-based dissipation term of Ardhuin et al. (2010), and the acceptable results obtained here, this parameterization appears to be

robust and should be preferred, also in cases with strong currents.

At larger scales, other effects are generally dominant, in particular the focusing of wave energy due to refraction over the currents. In these cases, the choice of dissipation parameterization, either Bidlot et al. (2005) or Ardhuin et al. (2010) has no noticeable impact, as long as a single wave system is present, for example, one swell or one wind sea.

We have found it particularly difficult to obtain or define current fields with spatial patterns that are accurate enough to give good wave model results. Surface currents observed by HF radars and obtained via standard processing routines can be too smooth to resolve the local but very strong current gradients that give large refraction effects. Here we have used a high-resolution tidal model, validated with high-resolution HF radar data to obtain a trustworthy current field. With this current field, numerical wave models such as WAVEWATCH III are capable of representing wave effects that occur in oceanic conditions, with a high degree of accuracy. Including currents in the model resulted in error reductions by up to 30%, even at locations where current are relatively weak but which are located down-wave of strong current gradients that cause large refraction effects. There may be significant differences between the results of different models due to different numerical techniques used for the integration of the wave action equation. This question has not been investigated here, but the reader may consult other publications (Roland 2008; Gonzalez-Lopez et al. 2011).

Finally, for short wind waves, results are very sensitive to the application of a correction on the wave-generating wind to use the relative wind, here defined as the vector difference of the 10-m height wind and the depth-averaged current. The modeling of this effect enhances the overall effects of currents with stronger tidal modulation that is qualitatively closer to the observations, although in our case it increased the model error because of a time shift of this modulation between the model and the observations. In our investigation of tidal currents, it is not possible to separate this relative wind effect from wave advection and growth effects.

Acknowledgments. Initial field and modeling work was initially funded by the French Navy EPEL Program (2002-2006), with additional help from CETMEF. The help of G. Amis (CETMEF), D. Corman (SHOM), and the crew of the hydrographic vessel *Laplace* are gratefully acknowledged. A.-C. B. acknowledges the support of a postdoctoral grant from INSU as part as the ANR-funded Project EPIGRAM, and F.A. is supported by a FP7-ERC young investigator Grant 240009 for the IOWAGA project, and U.S. National Ocean Partnership Program, under Grant N00014-10-1-0383. This work was also supported by FP7 program FIELD-AC. HF radar data were kindly provided by SHOM (http://www.shom.fr) as part of the Previmer project. Anonymous reviewers are thanked for helping in improving the paper.

REFERENCES

Alves, J. H. G. M., and M. L. Banner, 2003: Performance of a saturation-based dissipation-rate source term in modeling the fetch-limited evolution of wind waves. *J. Phys. Oceanogr.,* **33,** 1274–1298.

——, ——, and I. R. Young, 2003: Revisiting the Pierson–Moskowitz asymptotic limits for fully developed wind waves. *J. Phys. Oceanogr.,* **33,** 1301–1323.

Ardhuin, F., and R. Magne, 2007: Current effects on scattering of surface gravity waves by bottom topography. *J. Fluid Mech.,* **576,** 235–264.

——, T. H. C. Herbers, and W. C. O'Reilly, 2001: A hybrid Eulerian–Lagrangian model for spectral wave evolution with application to bottom friction on the continental shelf. *J. Phys. Oceanogr.,* **31,** 1498–1516.

——, ——, P. F. Jessen, and W. C. O'Reilly, 2003: Swell transformation across the continental shelf. Part II: Validation of a spectral energy balance equation. *J. Phys. Oceanogr.,* **33,** 1940–1953.

——, ——, K. P. Watts, G. P. van Vledder, R. Jensen, and H. Graber, 2007: Swell and slanting fetch effects on wind wave growth. *J. Phys. Oceanogr.,* **37,** 908–931.

——, L. Marié, N. Rascle, P. Forget, and A. Roland, 2009: Observation and estimation of Lagrangian, Stokes, and Eulerian currents induced by wind and waves at the sea surface. *J. Phys. Oceanogr.,* **39,** 2820–2838.

——, and Coauthors, 2010: Semi-empirical dissipation source functions for wind-wave models. Part I: Definition, calibration, and validation. *J. Phys. Oceanogr.,* **40,** 1917–1941.

——, J. Hanafin, Y. Quilfen, B. Chapron, P. Queffeulou, M. Obrebski, J. Sienkiewicz, and D. Vandemark, 2011a: Calibration of the IOWAGA global wave hindcast (1991–2011) using ECMWF and CFSR winds. *Proc. 12th Int. Workshop of Wave Hindcasting and Forecasting,* Hilo, HI, Environment Canada, 13 pp.

——, E. Stutzmann, M. Schimmel, and A. Mangeney, 2011b: Ocean wave sources of seismic noise. *J. Geophys. Res.,* **116,** C09004, doi:10.1029/2011JC006952.

——, J. Tournadre, P. Queffelou, and F. Girard-Ardhuin, 2011c: Observation and parameterization of small icebergs: Drifting breakwaters in the southern ocean. *Ocean Modell.,* **39,** 405–410, doi:10.1016/j.ocemod.2011.03.004.

Babanin, A. V., K. N. Tsagareli, I. R. Young, and D. J. Walker, 2010: Numerical investigation of spectral evolution of wind waves. Part II: Dissipation term and evolution tests. *J. Phys. Oceanogr.,* **40,** 667–683.

Banner, M. L., and R. P. Morison, 2006: On modeling spectral dissipation due to wave breaking for ocean wind waves. *Proc. Ninth Int. Workshop on Wave Hindcasting and Forecasting,* Victoria, BC, Canada, JCOMM, 12 pp.

——, and ——, 2010: Refined source terms in wind wave models with explicit wave breaking prediction. Part I: Model framework and validation against field data. *Ocean Modell.,* **33,** 177–189, doi:10.1016/j.ocemod.2010.01.002.

——, A. V. Babanin, and I. R. Young, 2000: Breaking probability for dominant waves on the sea surface. *J. Phys. Oceanogr.,* **30,** 3145–3160.

Barber, N. F., 1949: Behaviour of waves on tidal streams. *Proc. Roy. Soc. London,* **A198,** 81–93.

Battjes, J. A., 1982: A case study of wave height variations due to currents in a tidal entrance. *Coastal Eng.,* **6,** 47–57.

Benoit, M., F. Marcos, and F. Becq, 1996: Development of a third generation shallow-water wave model with unstructured spatial meshing. *Proc. 25th Int. Conf. on Coastal Engineering,* Orlando, FL, ASCE, 465–478.

Bidlot, J.-R., S. Abdalla, and P. Janssen, 2005: A revised formulation for ocean wave dissipation in CY25R1. ECMWF Research Department Tech. Rep. Memo. R60.9/JB/0516, 35 pp.

——, and Coauthors, 2007: Inter-comparison of operational wave forecasting systems. *Proc. 10th Int. Workshop of Wave Hindcasting and Forecasting,* Hilo, HI, Environment Canada, 22 pp. [Available online at http://www.waveworkshop.org/10thWaves/Papers/paper_10th_workshop_Bidlot_at_al.pdf.]

Chabert d'Hières, G., and C. Le Provost, 1970: Determination des characteristiques des ondes harmoniques m2 et m4 dans la manche sur modele reduit hydraulique. *C. R. Acad. Sci. Paris,* **A270,** 1703–1706.

Chawla, A., and J. T. Kirby, 2002: Monochromatic and random wave breaking at blocking points. *J. Geophys. Res.,* **107,** 3067, doi:10.1029/2001JC001042.

Cochin, V., V. Mariette, P. Broche, and R. Garello, 2006: Tidal current measurements using VHF radar and ADCP in the Normand Breton gulf: Comparison of observations and numerical model. *IEEE J. Oceanic Eng.,* **31,** 885–893.

Collard, F., F. Ardhuin, and B. Chapron, 2005: Extraction of coastal ocean wave fields from SAR images. *IEEE J. Oceanic Eng.,* **30,** 526–533.

Dobson, R. S., 1967: Some applications of a digital computer to hydraulic engineering problems. Stanford University Department of Civil Engineering Tech. Rep. 80, 114 pp.

Filipot, J.-F., and F. Ardhuin, 2012: A unified spectral parameterization for wave breaking: From the deep ocean to the surf zone. *J. Geophys. Res.,* **117,** C00J08, doi:10.1029/2011JC007784.

Forget, P., P. Broche, and F. Cuq, 1995: Principles of swell measurements by SAR with applications to ERS-1 observations off the Mauritanian coast. *Int. J. Remote Sens.,* **16,** 2403–2422.

Girard-Becq, F., B. Seillé, M. Benoit, F. Bazou, and F. Ardhuin, 2005: Evaluation of wave and current models from EPEL-GNB 2003 observations. *Proc. Fourth Int. Conf. EuroGOOS,* Brest, France, European Commission, 793–796.

Gonzalez-Lopez, J. O., J. Westerink, A. Mercado, J. Capella, J. Morell, and M. Canals, 2011: Effect of a steep and complex-featured shelf on computed wave spectra. *Proc. 12th Int. Workshop of Wave Hindcasting and Forecasting,* Hilo, HI, Environnement Canada, 1–4.

Gurgel, K.-W., G. Antonischki, H.-H. Essen, and T. Schlick, 1999: Wellen radar (WERA), a new ground-wave based HF radar for ocean remote sensing. *Coastal Eng.,* **37,** 219–234.

Hasselmann, K., 1974: On the spectral dissipation of ocean waves due to white capping. *Bound.-Layer Meteor.,* **6,** 107–127.

Haus, B. K., 2007: Surface current effects on the fetch-limited growth of wave energy. *J. Geophys. Res.,* **112,** C03003, doi:10.1029/2006JC003924.

Hedges, T. S., K. Anastasiou, and D. Gabriel, 1985: Interaction of random waves and currents. *J. Waterw. Port Coastal Ocean Eng.,* **111,** 275–288.

Holthuijsen, L., N. Booij, and T. Herbers, 1991: A prediction model for stationary, short-crested waves in shallow water with ambient currents. *Coastal Eng.,* **13,** 23–54.

Komen, G. J., K. Hasselmann, and S. Hasselmann, 1984: On the existence of a fully developed windsea spectrum. *J. Phys. Oceanogr.,* **14,** 1271–1285.

Kudryavtsev, V. N., S. A. Grodsky, V. A. Dulov, and A. N. Bol'shakov, 1995: Observations of wind waves in the Gulf Stream frontal zone. *J. Geophys. Res.,* **100** (C10), 20 715–20 727.

Lai, R. J., S. R. Long, and N. E. Huang, 1989: Laboratory studies of wave-current interaction: Kinematics of the strong interaction. *J. Geophys. Res.,* **94** (C11), 16 201–16 214.

Lazure, P., and F. Dumas, 2008: An external-internal mode coupling for a 3D hydrodynamical model for applications at regional scale (MARS). *Adv. Water Resour.,* **31,** 233–250.

Le Boyer, A., G. Cambon, N. Daniault, S. Herbette, B. L. Cann, L. Marié, and P. Morin, 2009: Observations of the ushant tidal front in September 2007. *Cont. Shelf Res.,* **29,** 1026–1037.

Lyard, F., F. Lefevre, T. Letellier, and O. Francis, 2006: Modelling the global océan tides: Modern insights from fes2004. *Ocean Dyn.,* **56,** 394–415.

Masson, D., 1996: A case study of wave-current interaction in a strong tidal current. *J. Phys. Oceanogr.,* **26,** 359–372.

Mathiesen, M., 1987: Wave refraction by a current whirl. *J. Geophys. Res.,* **92** (C4), 3905–3912.

McKee, W. D., 1978: The reflection of water waves by a shear current. *Pure Appl. Geophys.,* **115,** 937–949.

O'Reilly, W. C., and R. T. Guza, 1991: Comparison of spectral refraction and refraction-diffraction wave models. *J. Waterw. Port Coastal Ocean Eng.,* **117,** 199–215.

——, and ——, 1993: A comparison of two spectral wave models in the Southern California Bight. *Coastal Eng.,* **19,** 263–282.

Peregrine, D. H., 1976: Interaction of water waves and currents. *Adv. Appl. Mech.,* **16,** 9–117.

Phillips, O. M., 1977: *The Dynamics of the Upper Ocean.* Cambridge University Press, 336 pp.

——, 1984: On the response of short ocean wave components at a fixed wavenumber to ocean current variations. *J. Phys. Oceanogr.,* **14,** 1425–1433.

——, 1985: Spectral and statistical properties of the equilibrium range in wind-generated gravity waves. *J. Fluid Mech.,* **156,** 505–531.

Rascle, N., F. Ardhuin, P. Queffeulou, and D. Croizé-Fillon, 2008: A global wave parameter database for geophysical applications. Part 1: Wave-current-turbulence interaction parameters for the open ocean based on traditional parameterizations. *Ocean Modell.,* **25,** 154–171, doi:10.1016/j.ocemod.2008.07.006.

Ris, R. C., N. Booij, and L. H. Holthuijsen, 1999: A third-generation wave model for coastal regions. 2. Verification. *J. Geophys. Res.,* **104** (C4), 7667–7681.

Roland, A., 2008: Development of WWM II: Spectral wave modelling on unstructured meshes. Ph.D. thesis, Technische Universität Darmstadt, Institute of Hydraulic and Water Resources Engineering, 196 pp.

Saha, S., and Coauthors, 2010: The NCEP Climate Forecast System Reanalysis. *Bull. Amer. Meteor. Soc.,* **91,** 1015–1057.

Schmidt, R. O., 1986: Multiple emitter location and signal parameter estimation. *IEEE Trans. Antennas Propag.,* **AP-34,** 276–280.

Sentchev, A., P. Forget, and Y. Barbin, 2009: Residual and tidal circulation revealed by VHF radar surface current measurements

in the southern Channel Isles region (English Channel). *Estuarine Coastal Shelf Sci.,* **82,** 180–192.

——, ——, and M. Yaremchuk, 2012: Surface circulation in the Iroise Sea (W. Brittany) from high resolution HF radar mapping. *J. Mar. Syst.,* doi:10.1016/j.jmarsys.2011.11.024, in press.

Tolman, H. L., 1991a: Effects of tides and storm surges on North Sea wind waves. *J. Phys. Oceanogr.,* **21,** 766–781.

——, 1991b: A third generation model for wind on slowly varying, unsteady and inhomogeneous depth and currents. *J. Phys. Oceanogr.,* **21,** 766–781.

——, 2008: A mosaic approach to wind wave modeling. *Ocean Modell.,* **25,** 35–47, doi:10.1016/j.ocemod.2008.06.005.

——, 2009: User manual and system documentation of WAVEWATCH-III version 3.14. NOAA/NWS/NCEP/MMAB Tech. Rep. 276, 220 pp. [Available online at http://polar.ncep.noaa.gov/mmab/papers/tn276/276.xml.]

——, and D. Chalikov, 1996: Source terms in a third-generation wind wave model. *J. Phys. Oceanogr.,* **26,** 2497–2518.

——, and N. Booij, 1998: Modeling wind waves using wavenumber-direction spectra and a variable wavenumber grid. *Global Atmos. Ocean Syst.,* **6,** 295–309.

van der Westhuysen, A. J., M. Zijlema, and J. A. Battjes, 2005: Implementation of local saturation-based dissipation in SWAN. *Proc. Fifth Int. Symp. Ocean Wave Measurement and Analysis,* Madrid, Spain, ASCE, 1–10.

van Vledder, G. P., and D. P. Hurdle, 2002: Performance of formulations for whitecapping in wave prediction models. *Proc. OMAE.02 21st Int. Conf. on Offshore Mechanics and Artic Engineering,* Oslo, Norway, OMAE, OMAE2002-28146.

Vincent, C. E., 1979: The interaction of wind-generated sea waves with tidal currents. *J. Phys. Oceanogr.,* **9,** 748–755.

WAMDI Group, 1988: The WAM model—A third generation ocean wave prediction model. *J. Phys. Oceanogr.,* **18,** 1775–1810.

Waseda, T., T. Kinoshita, and H. Tamura, 2009: Evolution of a random directional wave and freak wave occurrence. *J. Phys. Oceanogr.,* **40,** 621–639.

WISE Group, 2007: Wave modelling—The state of the art. *Prog. Oceanogr.,* **75,** 603–674, doi:10.1016/j.pocean.2007.05.005.

Wolf, J., and D. Prandle, 1999: Some observations of wave–current interaction. *Coastal Eng.,* **37,** 471–485.